



OPEN

A thin film optoelectronic photodetector of spherical and linear resonators via one-pot synthesis of Bi(III) oxide/polypyrrole nanocomposite

Fatemah H. Alkallas¹, Mohamed Rabia², Fedor V. Kusmartsev^{3,4} & Amira Ben Gouider Trabelsi¹✉

We report the fabrication and characterization of a Bi(III) oxide/polypyrrole ($\text{Bi}_2\text{O}_3/\text{Ppy}$) nanocomposite thin film optoelectronic photodetector synthesized by a simple one-pot method. The nanocomposite consists of spherical Bi_2O_3 nanoparticles embedded in a Ppy matrix, forming a porous structure with a high surface area. The XRD analysis reveals that the Bi_2O_3 nanoparticles have a poly-crystalline nature with a crystal size of 40 nm and an optical bandgap of 2.86 eV. The SEM images show that the nanoparticles are agglomerated into clusters of about 100 nm in diameter, with pores of about 200 nm in width. The device exhibits a high sensitivity to light, as evidenced by the increase of the photocurrent density (J_{ph}) from -0.06 mA.cm^{-2} in the dark to -0.12 mA.cm^{-2} under illumination at -2.0 V. The device also shows a wavelength-dependent response, with the highest responsivity (R) of 1.0 and 0.9 mA/W and detectivity (D) of 0.221×10^9 and 0.20×10^9 Jones at photon energies of 3.6 eV and 2.8 eV, respectively. The $\text{Bi}_2\text{O}_3/\text{Ppy}$ nanocomposite is a promising material for low-cost, high-performance optoelectronic applications, making it a superior choice over many contemporary devices reported in recent literature.

Keywords Bi_2O_3 , Polypyrrole, Optoelectronic, Photodetector, High efficiency

The core working principle of various optoelectronic devices is based on their capacity to generate an electron-hole pair upon light absorption, which then leads to a current signal. There has been significant research interest in optoelectronic devices in recent years across diverse areas such as military applications, telecommunications, and medical services. This increased attention is mainly due to the unique structural and electrical properties of nanomaterials used in these devices¹⁻³.

Oxide semiconductors like ZnO and TiO_2 have historically been crucial in fabricating optoelectronic devices. They are appreciated for their high stability, ease of mass production, cost-effectiveness, and non-toxic characteristics. However, these materials have experienced limitations due to their low mobility and high recombination rates, which have restricted their broader application^{4,5}.

Researchers have developed new high-potential materials, such as bismuth-based compounds, to address these shortcomings. These materials find wide-ranging applications, including energy storage and sensor technologies. Bismuth materials are especially notable for their use in hydrogen storage and optoelectronic devices⁶. Additionally, the demand for semiconductor materials such as polymers has surged recently due to their cost-effectiveness and significant potential, making them valuable in various applications⁷⁻⁹.

Polypyrrole (Ppy) is a promising polymer because of its excellent electrical properties and strong UV region light absorbance. Various previous studies have explored different optoelectronic materials for polymer applications, such as TiO_2 -PANI¹⁰, fullerene materials like PBBTPD: Tri-PC61BM¹¹, oxide materials like $\text{ZnO}/\text{Cu}_2\text{O}$ ¹² and $\text{GO}/\text{Cu}_2\text{O}$ ¹³, and halide materials like $\text{PbI}_2\text{-}5\%\text{Ag}$ ⁸. Still, most of these studies reported R-values ranging between 0.0001 and 0.1 mA/W.

¹Department of Physics, College of Science, Princess Nourah bint Abdulrahman University, P.O. Box 84428, Riyadh 11671, Saudi Arabia. ²Nanomaterials Science Research Laboratory, Chemistry Department, Faculty of Science, Beni-Suef University, Beni-Suef 62514, Egypt. ³Physics Department, Khalifa University, Abu Dhabi, UAE. ⁴Physics Department, Loughborough University, Loughborough LE11 3TU, UK. ✉email: aatrabelsi@pnu.edu.sa

Establishing an optoelectronic device that provides a broad optical spectrum and high sensitivity and employs cost-effective, scalable production techniques presents an exciting challenge. Herein, the one-pot synthesis of the $\text{Bi}_2\text{O}_3/\text{Ppy}$ nanocomposite signifies a significant advancement in optoelectronic devices tailored for the UV-optical spectrum. With promising crystalline size, bandgap, and particle dimensions, this composite is ideal for fabricating photodetector devices. The performance of this optoelectronic device is evaluated under white light and various photon energies ranging from 3.6 to 2.3 eV, using J_{ph} values as sensitivity indicators. Efficiency is assessed by comparing J_{ph} and J_{o} values, while parameters like R and D measure overall device effectiveness. By integrating efficiency, sensitivity, and cost-effective mass production methods, this fabricated optoelectronic device holds considerable potential for industrial applications in optoelectronics.

Main properties of material composed of spherical and linear optical resonators

Functional metamaterials composed of Optical Resonators ranging in size from 100 to 400 nm display unique optoelectronic properties. Such structures within the material confine light, whether by reflection or refraction, prolonging the interaction between light and the material. Resonators constructed with precise dimensions, such as spherical resonators with about 100 nm diameters and linear resonators measuring approximately 400 nm, as formed for this study, can demonstrate distinctive and improved optoelectronic characteristics.

Increased light-matter Interaction

Localized Surface Plasmon Resonance (LSPR): Spherical resonators with a size of 100 nm may facilitate localized surface plasmons, which are collective electron oscillations on the material's surface. These plasmons result in significant light absorption and scattering at specific wavelengths, thus boosting light-matter interaction.

Whispering Gallery Modes (WGMs): Both types of resonators could support WGMs, allowing light to travel around the circumference of the resonator. This would lead to high-Q-factor resonances, indicating that the light remains confined with minimal loss and can circulate multiple times within the resonator. The resonance wavelength for LSPR in spherical resonators relies heavily on resonator size. A sphere with a 100 nm diameter tends to have a plasmon resonance beyond the UV range. Resonance enters the UV spectrum as diameters shrink below 100 nm, with the plasmon resonance moving to shorter wavelengths. There is also field enhancement, which depends on the size of the resonators. This is assigned to the electromagnetic field concentration that increases at shorter wavelengths with smaller resonators, leading to more terrific local field enhancement. This consequently improved light absorption and scattering at these wavelengths. Regarding spherical and linear resonators, size also influences the number and distribution of supported WGMs. Smaller resonators confine light more effectively, allowing higher-order modes at shorter wavelengths. A 100 nm spherical resonator will possess a denser mode structure in the UV spectrum than larger resonators. About the Quality Factor (Q-factor) of resonators, note that even though smaller resonators might see slightly reduced Q-factors because of heightened surface scattering, they still significantly confine modes and enhance fields at UV wavelengths.

Wide spectral responsivity

Multimode Resonance: A mix of spherical and linear resonators can sustain several resonance modes over an extensive spectral range, including visible to near-infrared (NIR) light, making the material sensitive to various light wavelengths, suitable for broadband photodetectors or sensors. The broad Spectral Responsivity may be changed by adjustment of Resonance Peaks: Modulating the size of resonators allows for customizable spectral responses. Smaller resonators near 100 nm demonstrate resonance peaks deep within the UV spectrum (below 300 nm). Conversely, 400 nm-sized resonators resonate in the near-UV to visible span (300–400 nm).

Employing variously sized resonators can expand the overall spectral sensitivity, promoting efficient light capture throughout the UV spectrum (100–400 nm). In addition, there appears to be Enhanced Photocurrent Production and Absorption Efficacy: Near 100 nm-sized resonators absorb shorter wavelengths (100–200 nm) more effectively, which could further increase photo-induced electron-hole pair production at these wavelengths. Therefore, altering the size of the resonators or the distance between them can tune the resonance wavelengths, enabling the design of materials with specific optical responses for a desired application.

Enhanced generation of photocurrent

Increased Absorption of Light: The resonators can trap light more effectively, thus increasing light absorption within the material. This may enhance electron-hole pairs' appearance and improve photocurrent in photodetectors or solar cells. **Generation of Hot Electrons:** Intense plasmonic fields at the surfaces of resonators can produce hot electrons, which are high-energy electrons that can be collected to enhance photocurrent and efficiency in photodetectors and photovoltaic technologies. As hot electron production improves at resonance wavelengths, smaller-tuned resonators are more proficient at generating these electrons at UV wavelengths, benefiting the photocurrent.

Greater sensitivity and detectivity

Field Enhancement: Due to the confinement of light, the electromagnetic field is substantially enhanced close to the surfaces of the resonators. This improves the material's sensitivity to environmental changes like refractive index variations, which is beneficial for sensing devices.

Nonlinear Optical Effects: The intense field strength can trigger nonlinear optical phenomena, such as second-harmonic generation or two-photon absorption, making the material suitable for sophisticated optoelectronic applications like frequency conversion or optical modulation.

Sensitivity to Resonance Shifts: Size determines how sensitive resonators react to environmental changes. Small resonators indicate significant shifts in resonance wavelength for specific refractive index alterations, enhancing UV light detection sensitivity.

Improved charge transportation

Carrier Mobility: When embedded in a semiconductor matrix within a composite material, the resonators might provide adequate pathways for charge transport, enhancing carrier mobility and conductivity. While indirectly related, resonator size is pivotal in improving charge movement. **Impact on Carrier Mobility:** Smaller resonators, with more intensive field enhancements, originate more effective carrier pathways, particularly at UV wavelengths where the light interaction intensifies.

Reduced Recombination: By better spatially separating charge carriers with resonators, recombination rates can decrease, increasing device efficiency. **Nonlinear Optical Effects:** Due to the increased field intensity in smaller resonators, nonlinear phenomena like two-photon absorption become more notable at shorter wavelengths. There is a minimization of recombination in smaller resonators; the separation of charge carriers is more productive, reducing recombination rates and heightening the efficiency of UV-based optoelectronic devices.

Experimental section

Materials and characterization

Bismuth nitrate ($\text{Bi}(\text{NO}_3)_3 \cdot 5\text{H}_2\text{O}$, 99.9%, sourced from Merck, Germany), pyrrole (99.9%, from Merck, Germany), DMF (99.9%, procured from Sigma Aldrich, USA), hydrochloric acid (HCl, 36%, supplied by Pio-Chem, Egypt), and ammonium persulfate ($(\text{NH}_4)_2\text{S}_2\text{O}_8$, 99.8%, obtained from Pio-Chem, Egypt).

The characterization process is carried out using different instruments depending on the type of analysis: chemical analyses are conducted with FTIR using a Bruker instrument, XPS using a Kratos instrument, and XRD using an X'Pert instrument. For 2D imaging, a TEM (Joel) device is used, while 3D imaging is performed with an SEM (Zeiss) instrument. Optical analyses are carried out using a Perkin Elmer device.

The one-pot synthesizing of Bi_2O_3 /Ppy nanocomposite thin film

The Bi_2O_3 /Ppy nanocomposite is synthesized using a one-pot method, where the bismuth source is incorporated into the pyrrole monomer during the polymerization phase. The procedure begins by thoroughly dissolving 0.06 M pyrrole in 5 ml of HCl, making up a total volume of 50 ml. Subsequently, 0.06 M $\text{Bi}(\text{NO}_3)_3 \cdot 5\text{H}_2\text{O}$ is added to this monomer solution, facilitated by adding 10 ml of HCl while stirring at room temperature until the solution becomes evident. Simultaneously, the oxidant, $(\text{NH}_4)_2\text{S}_2\text{O}_8$, is dissolved in distilled water (0.13 M) while stirring at 25 °C. The oxidant solution is then quickly added to the monomer mixture, initiating the polymerization process. Bi_2O_3 is incorporated into the forming Ppy, resulting in the Bi_2O_3 /Ppy composite. A glass substrate is used to create a uniform thin film of the Bi_2O_3 /Ppy nanocomposite. The synthesis aims to produce a highly homogeneous Bi_2O_3 /Ppy nanocomposite thin film through a controlled integration of the components. Finally, the film is dried and treated for subsequent application procedures.

The electrical testing of Bi_2O_3 /Ppy nanocomposite thin film optoelectronic device

The electrical testing of the fabricated Bi_2O_3 /Ppy nanocomposite thin film optoelectronic device aims to verify its light-sensing capabilities and determine the range of optical spectra it utilizes. To conduct this testing, the fabricated thin film is prepared by fixing two silver (Ag) paste contacts on both sides of the optoelectronic film. This setup is then connected to a CHI608E electrochemical workstation to perform linear sweep voltammetry and chronoamperometry tests. These tests help estimate the photocurrent density (J_{ph}) values, which indicate the device's sensitivity to light.

All tests are conducted under a vacuum tube metal halide lamp, 400 W, which emits a complete white light spectrum. This setup allows the assessment of the device's photoresponsivity (R) and detectivity (D), crucial metrics for evaluating its performance across different optical spectra. As the optical spectra increase, the enhanced performance of the optoelectronic device is expected. The photoresponsivity (R) is calculated using Eq. 1¹⁴, which involves parameters such as the current density in different lighting conditions, from white light to darkness (J_0), and the incident light power (P). Equation 2 provides the detectivity (D)¹⁴, which relies on factors including the electron charge (e) and the active area of the optoelectronic device (A). Examining these parameters quantifies the device's sensitivity and efficiency in detecting light across various spectra. Higher R and D values indicate better performance and sensitivity, demonstrating the effectiveness of the Bi_2O_3 /Ppy nanocomposite thin film in optoelectronic applications. This estimation is confirmed, as illustrated in Fig. 1. To determine these parameters at different photon energies, external optical filters were employed to isolate wavelengths of 340, 440, and 540 nm, which correspond to energies of 3.6, 2.8, and 2.3 eV, respectively.

$$R = \frac{J_{\text{ph}} - J_0}{P} \quad (1)$$

$$D = R \sqrt{A/2eJ_0} \quad (2)$$

Results and discussion

Chemical analysis

Figure 2a illustrates the FTIR measurements for the Ppy polymer and the composite of Bi_2O_3 /Ppy. The various chemical groups identified in these materials are detailed in Table 1. A noticeable blue shift is observed when comparing the ring bonds in the Bi_2O_3 /Ppy composite to those in the pristine Ppy. For the Bi_2O_3 /Ppy composite, the ring bonds are located at 1631 cm^{-1} and 1550 cm^{-1} , and the C-N bond appears at 1399 cm^{-1} . In contrast, the pristine Ppy exhibits ring bonds at 1701 cm^{-1} , 1545 cm^{-1} , and 1463 cm^{-1} , with the C-N bonds at 1312 cm^{-1} . The primary Bi-O bond in the composite is observed at 611 cm^{-1} . These shifts and bond positions indicate the

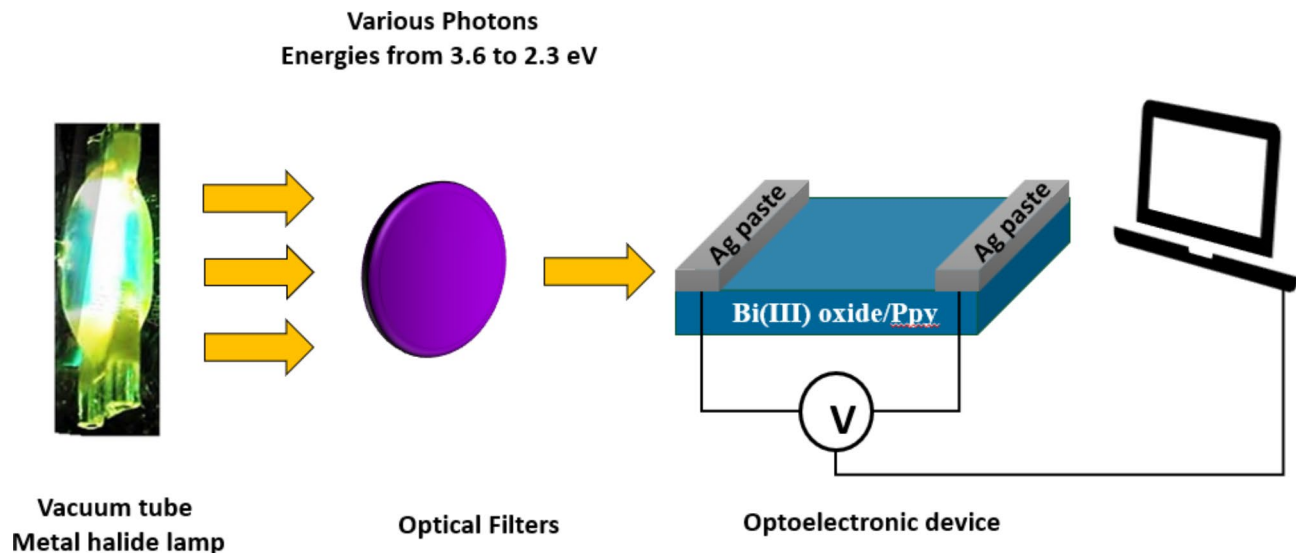


Fig. 1. The fabricated $\text{Bi}_2\text{O}_3/\text{Ppy}$ optoelectronic schematic diagram for UV-Vis light sensing.

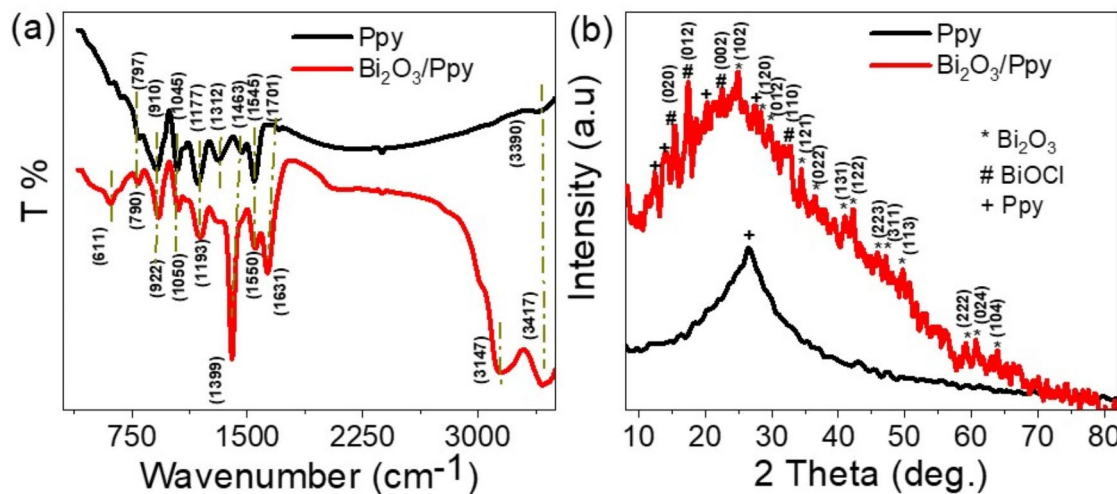


Fig. 2. The chemical and crystalline structure of the synthesized $\text{Bi}_2\text{O}_3/\text{Ppy}$ nanocomposite. **(a)** the FTIR data and **(b)** the XRD pattern, respectively.

Peak Position (cm^{-1})		Functional groups
Ppy	$\text{Bi}_2\text{O}_3/\text{Ppy}$	
1701, 1545, and 1463	1631 and 1550	Ppy ring
1312	1399	C-N [15]
1177	1193	C-H [16]
-	611	Bi-O

Table 1. The estimated bonds related to the FTIR with their positions in cm^{-1} .

successful formation of the $\text{Bi}_2\text{O}_3/\text{Ppy}$ composite, suggesting significant interactions between the bismuth oxide and the Ppy matrix.

The crystalline structure of the synthesized $\text{Bi}_2\text{O}_3/\text{Ppy}$ nanocomposite is characterized by examining the crystalline structure of its constituent materials using XRD (Fig. 2b). The XRD analysis reveals specific 2θ

positions for peaks associated with Bi_2O_3 , located at $63.9^\circ, 61.1^\circ, 58.9^\circ, 49.6^\circ, 47.3^\circ, 45.9^\circ, 42.1^\circ, 41.1^\circ, 36.4^\circ, 34.4^\circ, 29.6^\circ, 28.4^\circ$, and 24.8° . These peaks correspond to the Miller indices (104), (024), (222), (113), (311), (223), (122), (131), (022), (121), (012), (012), and (102), respectively, as per the JCPDS standard 76-1730^{17,18}. These peaks highlight the composite's crystallinity, suggesting its potential application in optoelectronics due to the wide sensitivity of its crystalline structures to incident photons.

The crystalline size of the materials is further determined using the Scherrer equation (Eq. 3)^{19,20}, which focuses on the prominent crystalline peak at $2\theta = 24.8^\circ$. The calculated crystal size (D) is approximately 40 nm, indicating a well-defined crystalline structure using the full-width half maximum (β). Additionally, there are minor peaks in the XRD pattern related to the BiOCl phase within the synthesized $\text{Bi}_2\text{O}_3/\text{Ppy}$ nanocomposite. These peaks are found at $30.8^\circ, 22.4^\circ, 18.3^\circ$, and 15.2° , corresponding to the Miller indices (110), (002), (012), and (020), respectively, as per JCPDS standard 06-0249²¹. These minor peaks suggest the presence of BiOCl structures within the composite. To better understand the behavior of this crystalline nanocomposite, it is compared to the pristine Ppy. The XRD pattern of pristine Ppy displays a broad peak, indicating its amorphous nature. In contrast, the sharp and well-defined peaks of the $\text{Bi}_2\text{O}_3/\text{Ppy}$ nanocomposite reflect its high crystallinity, which enhances its potential as an optoelectronic material due to its effective interaction with incident photons across a broad spectrum.

$$D = 0.9\lambda / \beta \cos\theta \quad (3)$$

To study the behavior and oxidation states of the Bi element within the $\text{Bi}_2\text{O}_3/\text{Ppy}$ nanocomposite, XPS analyses were performed, as shown in Fig. 3. The study reveals a single peak for the Bi element corresponding to the +3 oxidation state (Fig. 3b). The binding energies for $\text{Bi}4f_{7/2}$ and $\text{Bi}4f_{5/2}$ are observed at 159.7 eV and 165.1 eV,

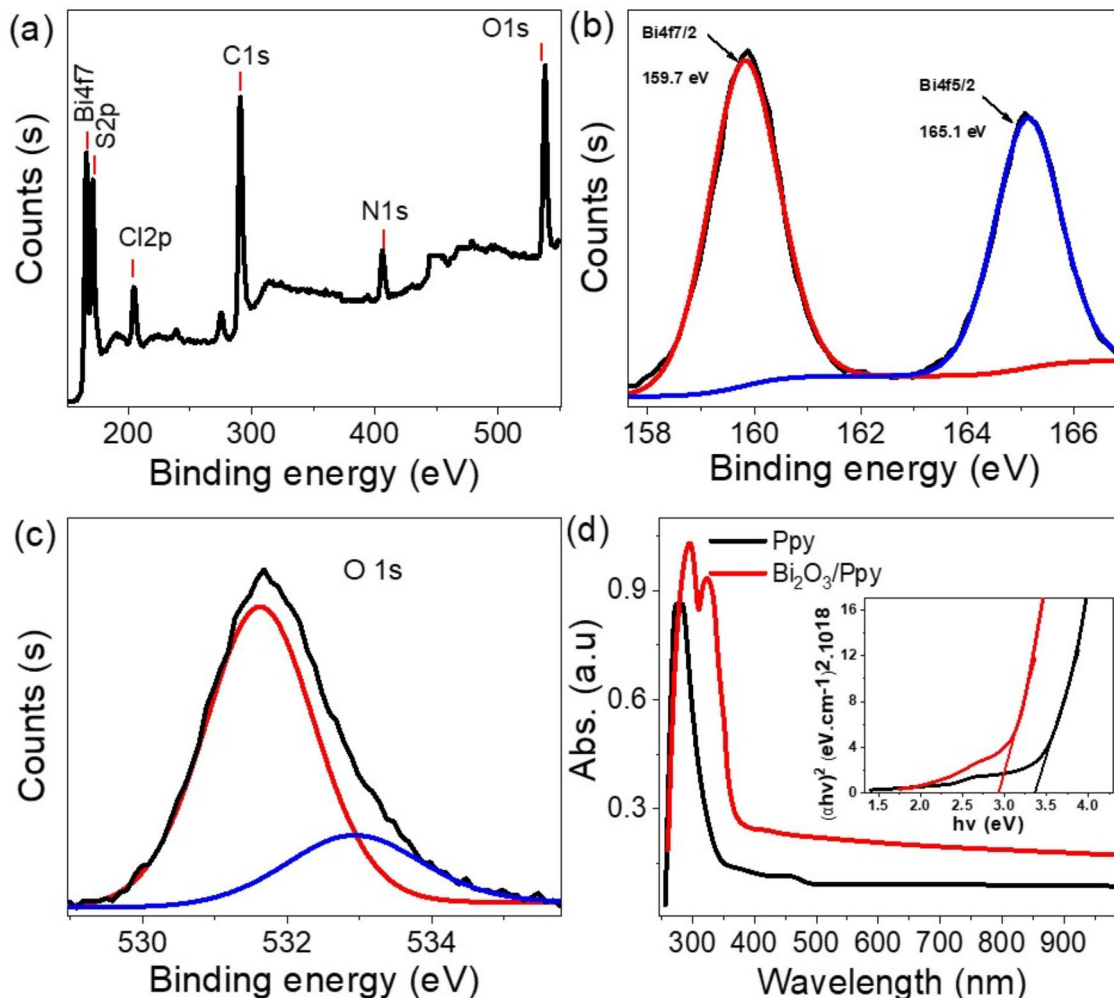


Fig. 3. (a-c) The characterizations of the synthesized $\text{Bi}_2\text{O}_3/\text{Ppy}$ nanocomposite were conducted using XPS, and (d) displayed the optical absorption properties of the nanocomposite compared to polypyrrole material. The inset figure provides the calculated bandgap estimation.

respectively. This single peak indicates the formation of Bi_2O_3 . The absence of additional peaks at these positions suggests that BiOCl is only a trace amount, not a significant component in the $\text{Bi}_2\text{O}_3/\text{Ppy}$ nanocomposite. The oxygen element is represented in Fig. 3c, where the O1s orbital peaks at 532 eV, indicating the presence of oxygen, a key component in Bi_2O_3 . Other elements are identified in the survey, as shown in Fig. 3a. Nitrogen is detected via its 1s orbital at 400 eV, and carbon is identified through its 1s orbital at 286 eV. The combination of these detected elements and the oxidation states of the Bi element confirms the successful formation of the $\text{Bi}_2\text{O}_3/\text{Ppy}$ nanocomposite. The elemental composition of the $\text{Bi}_2\text{O}_3/\text{Ppy}$ nanocomposite is determined using XPS, revealing the percentages of Bi, O, Cl, C, and N to be 2.27%, 17.64%, 9.85%, 61.98%, and 8.13%, respectively.

The optical behavior of the synthesized $\text{Bi}_2\text{O}_3/\text{Ppy}$ nanocomposite is depicted in Fig. 3d. This nanocomposite exhibits significant optical absorbance in the UV region, extending up to 390 nm, which is attributed to the high-intensity absorbance in this range²². A doublet peak in this region suggests a synergistic effect between Bi_2O_3 and Ppy materials during the $\text{Bi}_2\text{O}_3/\text{Ppy}$ nanocomposite formation. This absorbance is linked to electron transitions and the formation of electron clouds in the conduction band. This optical behavior is reflected in the evaluated bandgap, calculated to be 2.86 eV using the Tauc equation (Eq. 4)^{23,24}. This equation calculates the bandgap (E_g) values using the light frequency (ν) and the absorption coefficient (α). The calculation is based on additional parameters, such as the absorbance (A) and Planck's constant (h).

$$\alpha h\nu = A(h\nu - E_g)^{1/2} \quad (4)$$

The morphological and topographical characteristics of the synthesized $\text{Bi}_2\text{O}_3/\text{Ppy}$ nanocomposite significantly impact its optical properties. These characteristics were examined using SEM analyses, as shown in Fig. 4a,b at various magnifications. The SEM images reveal the presence of large agglomerated spherical nanoparticles approximately 100 nm in diameter, interspersed with wide pores around 200 nm in size. This structure is beneficial for enhancing photon localization and trapping, thereby increasing the surface area available for interactions.

The morphology of the $\text{Bi}_2\text{O}_3/\text{Ppy}$ nanocomposite resembles that of pristine Ppy, as shown in Fig. 4d. The Ppy consists of rough semi-spherical particles with an average size of 230 nm. The rough surface of Ppy facilitates the formation of the composite when reacted with Bi materials. The SEM images show that the $\text{Bi}_2\text{O}_3/\text{Ppy}$ nanocomposite maintains a similar rough and porous structure, which is advantageous for optoelectronic applications due to improved photon absorption and surface interactions^{3,25}.

TEM images provide further evidence of the successful preparation of the $\text{Bi}_2\text{O}_3/\text{Ppy}$ nanocomposite (see Fig. 4c). These images clearly show the presence of Bi_2O_3 within the Ppy polymer matrix, indicated by dark areas within the polymer (see Fig. 2d). The dark regions correspond to the Bi_2O_3 components, confirming their integration into the Ppy structure. This integration is crucial for the enhanced optical properties observed in the composite, as the presence of Bi_2O_3 and BiS within the Ppy matrix contributes to the synergistic effects that improve the material's overall performance in optoelectronic applications.

For further assessment of the film's cross-section, the thickness is determined using SEM combined with theoretical modeling, revealing a thickness of 300 nm (see Fig. 4e). The spherical particles are observed to be well-ordered, and the film exhibits a slight roughness with small porosity, which facilitates photon trapping.

The electrical testing of the fabricated $\text{Bi}_2\text{O}_3/\text{Ppy}$ thin film optoelectronic photodetector

The electrical testing of the fabricated $\text{Bi}_2\text{O}_3/\text{Ppy}$ thin film optoelectronic photodetector involves estimating the generated hot electrons under different light conditions. These conditions encompass a range of photon energies from 2.3 to 3.6 eV and white light. A vacuum tube metal halide lamp is employed as the white light source. At the same time, the specific photon energies are achieved using optical filters that allow only the desired photon frequencies to pass through.

The photodetector has a surface area of 1.0 cm^2 , and the electrical measurements are conducted at room temperature. For a comprehensive evaluation, Ag paste is applied to both sides of the film, serving as connection points to the electrochemical workstation CHI608E. Linear sweep voltammetry is then performed within a potential range of -2.0 to +2.0 V. This relatively low potential is suitable for assessing the hot electrons generated by the optoelectronic device.

Figure 5a illustrates the J_{ph} produced by the fabricated $\text{Bi}_2\text{O}_3/\text{Ppy}$ thin film photodetector under light illumination, registering -0.12 mA/cm^2 at a voltage of -2.0 V. This significant value highlights the efficient generation of hot electrons by the nano-semispherical thin film materials. The high J_{ph} indicates substantial energy level splitting between the Bi_2O_3 and Ppy materials. This leads to an accumulation of hot electrons on Bi_2O_3 due to its lower energy level than Ppy. The resultant electron clouds on Bi_2O_3 create a strong electric field within the composite material, driving the hot electrons to the external circuit of the optoelectronic device and regenerating the J_{ph} values.

In the absence of light, the device generates a J_o of less than 0.06 mA/cm^2 . This lower value demonstrates that the $\text{Bi}_2\text{O}_3/\text{Ppy}$ semiconductor composite still conducts electricity in the dark, though at a significantly reduced rate. The substantial difference between the illuminated J_{ph} and dark J_o values underscores the fabricated device's sensitivity and efficiency in light sensing and photon capture.

To evaluate the stability of the $\text{Bi}_2\text{O}_3/\text{Ppy}$ optoelectronic device, a reproducibility study was conducted under photon illumination over three runs, as shown in Fig. 5b. The device exhibited a standard deviation of less than 2%, indicating promising stability and potential for commercial applications. This robustness is attributed to the intrinsic properties of the materials used in fabrication: Bi_2O_3 , known for its high stability, and Ppy polymer, which offers excellent strength and anticorrosion characteristics.

The high stability of the $\text{Bi}_2\text{O}_3/\text{Ppy}$ optoelectronic device is due to the synergistic properties of these two materials. Bi_2O_3 , a highly stable substance, is embedded within the Ppy polymer matrix, enhancing the overall

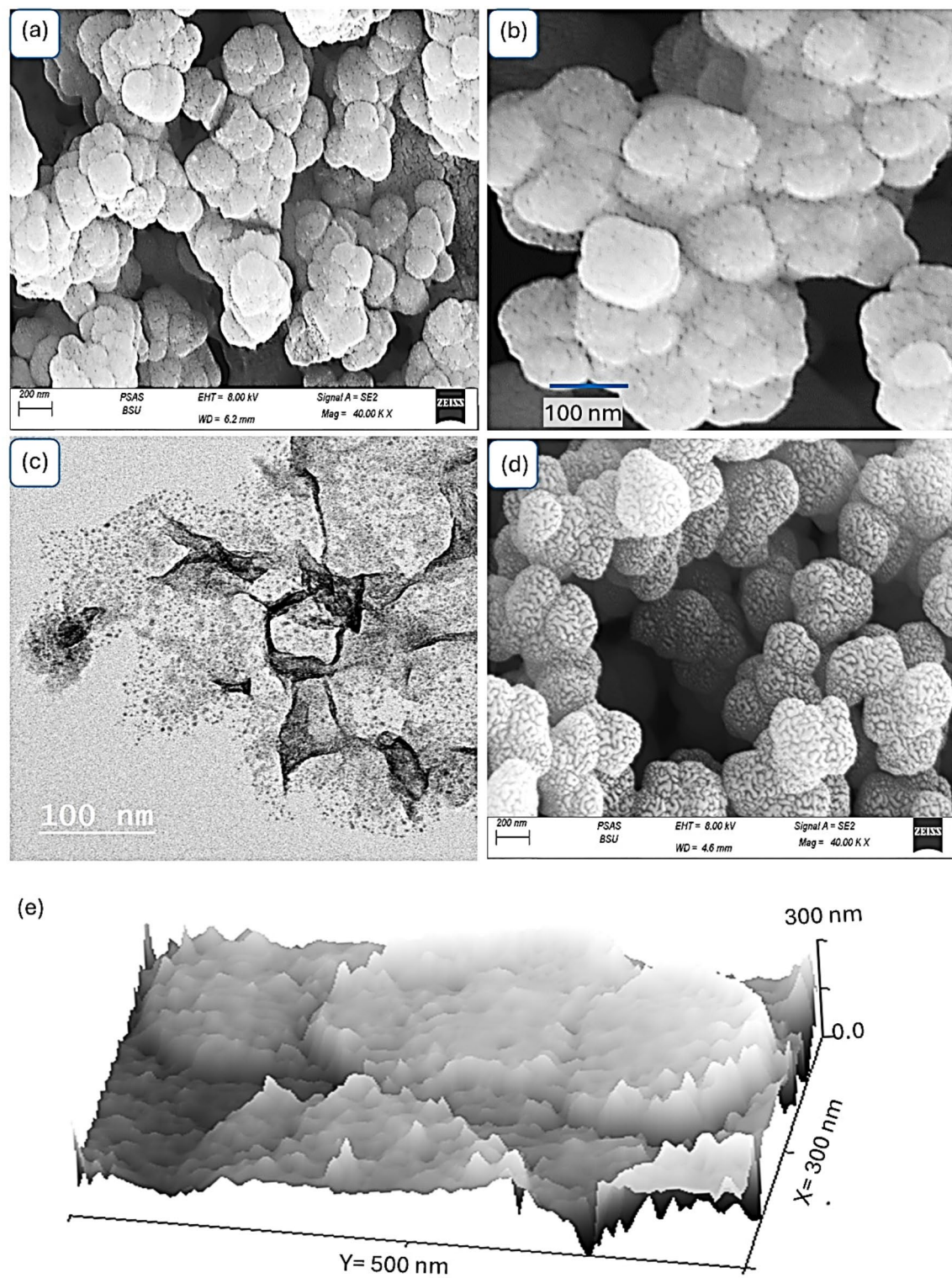


Fig. 4. Presents (a-b) the SEM images, (c) the TEM image, and (e) the modeling cross-section of the synthesized $\text{Bi}_2\text{O}_3/\text{Ppy}$ nanocomposite, along with (d) the SEM image of the pristine Ppy. The micrographs in panels (a-b) illustrate that the novel material comprises dense spherical and rod-like structures.

stability and durability of the composite material. The Ppy polymer's anticorrosion nature further contributes to the longevity and reliability of the device, making it suitable for various optoelectronic applications.

The study presented in Fig. 6a demonstrates the responsivity of the fabricated $\text{Bi}_2\text{O}_3/\text{Ppy}$ photodetector to different photon energies. The graph shows a significant variation in the generated J_{ph} under these varying photon energies. Specifically, the J_{ph} decreases from -0.1 to -0.07 mA.cm^{-2} as the photon energy decreases from

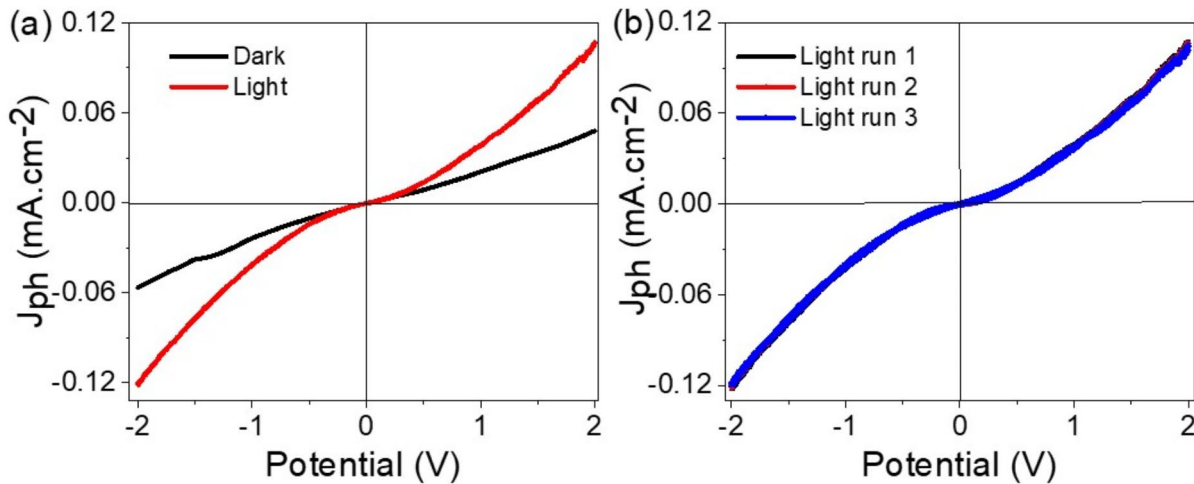


Fig. 5. (a) Displays the electrical linear sweep voltammetry (-2.0 to 2.0 V) of the created $\text{Bi}_2\text{O}_3/\text{Ppy}$ optoelectronic device, and (b) presents the consistency analysis over three lighting tests.

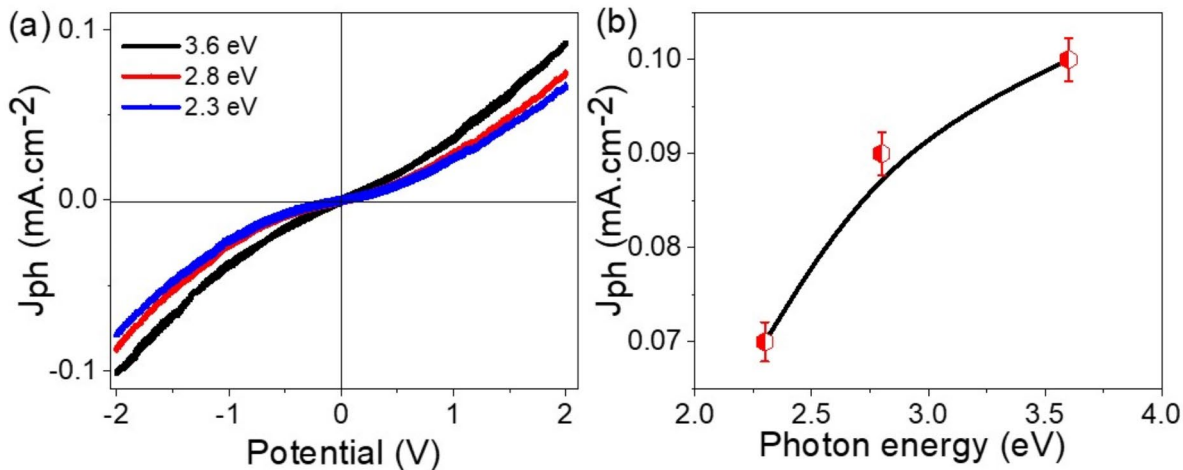


Fig. 6. Presents (a) the electrical linear sweep voltammetry results, spanning from -2.0 to 2.0 V, of the constructed $\text{Bi}_2\text{O}_3/\text{Ppy}$ optoelectronic device with photon energies varying between 2.3 and 3.6 eV, and (b) the calculated J_{ph} at a potential of -2.0 V.

3.6 eV to 2.3 eV. The highest values of J_{ph} are observed at photon energies of 3.6 eV and 2.8 eV, indicating optimal performance at these energies.

Figure 6b provides further insight into the J_{ph} values produced at these photon energies. The observed behavior suggests that photon energies of 3.6 eV and 2.8 eV are particularly effective in achieving complete electron excitation and transfer to the conducting energy level. This process results in the formation of an electric field that drives the hot electrons, thereby generating significant J_{ph} values at wavelengths of 340 nm and 440 nm, respectively. These findings suggest that the fabricated $\text{Bi}_2\text{O}_3/\text{Ppy}$ photodetector performs optimally within these photon energy regions. Consequently, it holds promise as an efficient optoelectronic photodetector for applications requiring sensitivity in these photon energy ranges.

The sensitivity of the fabricated $\text{Bi}_2\text{O}_3/\text{Ppy}$ optoelectronic device is determined by calculating the percentage of photons converted into hot electrons, assessed through the R-value as shown in Fig. 7a. The highest R-values are observed at 3.6 eV and 2.8 eV photon energies, with values of 1.0 and 0.9 mA/W. These values correlate with the D values at these photon energies, as depicted in Fig. 7b, which are 0.221×10^9 and 0.20×10^9 Jones, respectively.

These promising values underscore two significant points: firstly, the exceptional responsivity of this optoelectronic device to photons in the UV and the initial visible regions, and secondly, its superior performance

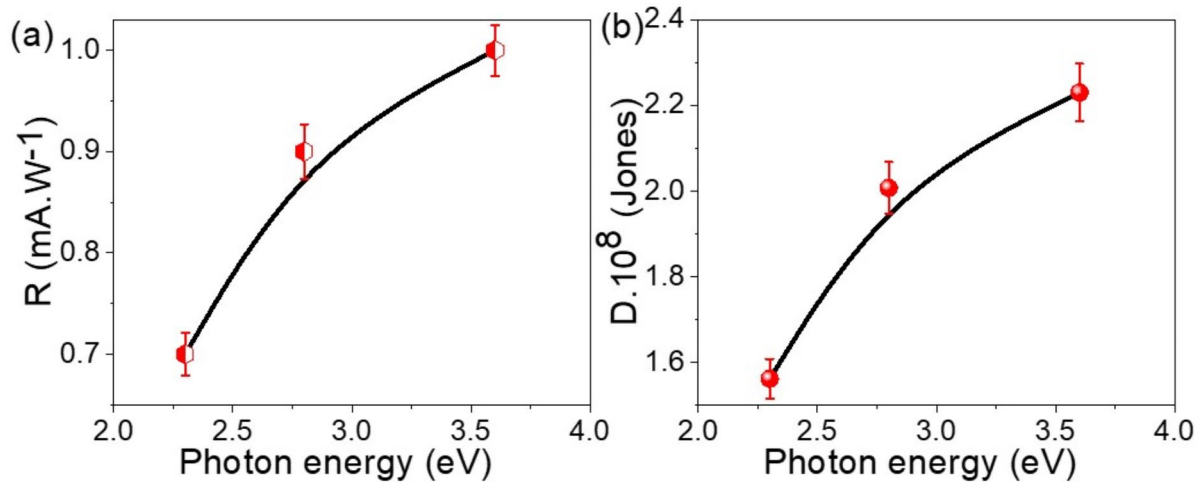


Fig. 7. Provides detailed characteristics of the fabricated $\text{Bi}_2\text{O}_3/\text{Ppy}$ optoelectronic device under different photon energies. Specifically, panel (a) illustrates the photoresponsivity, while panel (b) demonstrates the detectivity. The photon energies assessed range from 3.6 eV to 2.3 eV.

Optoelectronic device	Wavelength (nm)	Potential (V)	R (mA.W ⁻¹)
Bi_2O_3 ⁶	365	1	-
Ppy/CuO ²⁸	340	2	0.05
TiO_2 -PANI ¹⁰	320	0	3×10^{-3}
ZnO /RGO ²⁹	350	5	1.3×10^{-3}
PBBTPD: Tri-PC ₆₁ BM ¹¹	350	5	10^{-4}
Ppy/NiO _X ³⁰	340	2	0.07
ITO/CsPbBr ₃ -ZnO/Ag ²⁶	405	0	0.01
$\text{ZnO}/\text{Cu}_2\text{O}$ ³¹	350	2	4×10^{-3}
Graphene/GaN ³²	365	7	3×10^{-3}
GO/Cu ₂ O ¹³	300	2	0.5×10^{-3}
PC ₇₁ BM ²⁷	300	2	0.005
CuO nanowires ³³	390	5	-
TiN/TiO ₂ ³⁴	550	5	-
P3HT ³⁵	325	1	NA
CuO/Si Nanowire ³⁶	405	0.2	3.8×10^{-3}
PbI ₂ -5%Ag ⁸	532	6	NA
Carbon-Co ₃ O ₄ ³⁵	350	2	0.01
Se/TiO ₂ ³⁸	450	1	5×10^{-3}
ZnO -CuO ³⁹	405	1	3×10^{-3}
$\text{Bi}_2\text{O}_3/\text{Ppy}$ (this work)	340	2	1.0

Table 2. The extraordinary sensitivity dynamics of the innovatively engineered $\text{Bi}_2\text{O}_3/\text{Ppy}$ thin-film optoelectronic device, compared to prior studies, showcasing its unparalleled superiority and advanced championship qualities.

compared to other recent studies. For instance, devices such as PBBTPD: Tri-PC61BM, ITO/CsPbBr₃/Ag, and PC₇₁BM exhibit R-values ranging from approximately 0.01 to 0.0001 mA/W^{11,26,27}, as noted in the literature (see Table 2 for more details). This demonstrates that the fabricated $\text{Bi}_2\text{O}_3/\text{Ppy}$ device significantly outperforms these alternatives.

In summary, the $\text{Bi}_2\text{O}_3/\text{Ppy}$ optoelectronic device shows high sensitivity and excellent responsivity to UV and initial visible light, making it a superior choice over many contemporary devices reported in recent literature.

Conclusions

In conclusion, we describe the innovative material we discovered, composed of spherical optical resonators (with diameters starting at 100 nm) and linear resonators (sized around 400 nm). These nanocomposite materials exhibit unique and advanced optoelectronic characteristics due to their exceptional light confinement and interaction efficiency. Such attributes encompass increased light absorption, broad spectral responsivity, heightened sensitivity and detectability, superior photocurrent production, and enhanced charge transportation, presenting considerable potential for various applications, including sophisticated photodetectors, sensors, and photovoltaic systems. In the 100 to 400 nm wavelength spectrum, resonator size significantly influences the optoelectronic properties of spherical (100 nm) and linear (400 nm) resonators. Notably, smaller resonators are particularly adept at intensifying light-matter interactions at shorter wavelengths, leading to superior light absorption, field enhancement, generation of hot electrons, and device responsiveness. These effects significantly benefit UV-specific applications, such as advanced photodetectors and sensors. Customizing the resonator size permits a tailored approach to the material's optical properties, meeting specific needs within the UV spectrum.

Data availability

All data generated or analysed during this study are included in this published article.

Received: 3 September 2024; Accepted: 8 January 2025

Published online: 23 January 2025

References

1. Zhang, Q. et al. J 2023 Enhanced gain and detectivity of unipolar barrier solar blind avalanche photodetector via lattice and band engineering *Nat. Commun.* **14**.
2. Sreedhar, A., Ta, Q. T., H & Noh, J-S. Versatile role of 2D Ti3C2 MXenes for advancements in the photodetector performance: A review. *J. Ind. Eng. Chem.* (2023).
3. Nawar, A. M. & El-Mahalawy, A. M. Heterostructure device based on brilliant green nanoparticles–PVA/p-Si interface for analog–digital converting dual-functional sensor applications. *J. Mater. Sci.: Mater. Electron.* **31**, 3256–3273 (2020).
4. Wang, X. et al. Q 2022 high performance self-powered UV-visible photodetectors based on TiO₂/graphene/ZnIn₂S₄/electrolyte heterojunctions. *Ceram. Int.* **48**, 13090–13099
5. Zhan, T. et al. J 2023 electrical characteristics and photodetection mechanism of TiO₂/AlGaN/GaN heterostructure-based ultraviolet detectors with a Schottky junction. *J. Mater. Chem. C* **11**, 1704–1713
6. Ren, S. et al. J 2023 a simple solution synthesis of massive 2D triangular Bi₂O₃ nanosheets for self-powered UV photodetection. *Opt. Mater.* **135**, 113307
7. Elsayed, A. M. et al. 2023 Photodetection Enhancement via Graphene Oxide Deposition on Poly 3-Methyl Aniline *Micromachines* **2023**, Vol. **14**, Page 606 14606
8. Ismail, R. A., Mousa, A. M. & Shaker, S. S. Visible-enhanced silver-doped PbI₂ nanostructure/Si heterojunction photodetector: Effect of doping concentration on photodetector parameters. *Opt. Quant. Electron.* **51**, 1–19 (2019).
9. El-Mahalawy, A. M., Abd Rabou, M. M., Mansour, S. A. & Ali, F. M. Mechanistic exploration of charge transport and photosensitivity of metal/polymer/semiconductor (MPS) junction for sensitive light detection applications. *J. Mater. Sci.: Mater. Electron.* **34**, 1–23 (2023).
10. Zheng, L., Yu, P., Hu, K., Teng, F. & Chen, H. and Fang X 2016 Scalable-Production, self-powered TiO₂ Nanowell-Organic hybrid UV photodetectors with tunable performances. *ACS Appl. Mater. Interfaces* **8**, 33924–33932
11. Zheng, L. et al. F 2018 solution-processed broadband polymer photodetectors with a spectral response of up to 2.5 μm by a low bandgap donor–acceptor conjugated copolymer. *J. Mater. Chem. C* **6**, 3634–3641
12. Huang, G., Zhang, P. & Bai, Z. Self-powered UV-visible photodetectors based on ZnO/graphene/CdS/electrolyte heterojunctions. *J. Alloys Compd.* **776**, 346–352 (2019).
13. Lan, T., Fallatah, A., Suiter, E. & Padalkar, S. 2017 Size Controlled Copper (I) Oxide Nanoparticles Influence Sensitivity of Glucose Biosensor *Sensors* **17** (1944).
14. Rabia, M., Aldosari, E. & Abdelazeez, A. A. A. An advanced optoelectronic apparatus utilizing poly(2-amino thiophenol) adorned with a needle-shaped MnS-MnO₂ nanocomposite. *J. Mater. Sci.: Mater. Electron.* **35**, 1–12 (2024).
15. Hameed, S. A., Ewais, H. A. & Rabia, M. Dumbbell-like shape Fe₂O₃/poly-2-aminothiophenol nanocomposite for two-symmetric electrode supercapacitor application. *J. Mater. Sci.: Mater. Electron.* **34**, 1–8 (2023).
16. Azzam, E. M. S., Abd El-Salam, H. M. & Aboad, R. S. Kinetic preparation and antibacterial activity of nanocrystalline poly(2-aminothiophenol). *Polym. Bull.* **76**, 1929–1947 (2019).
17. Jabeen Fatima, M. J., Niveditha, C. V. & Sindhu, S. 2015 α-Bi₂O₃ photoanode in DSSC and study of the electrode–electrolyte interface. *RSC Adv.* **5** 78299–78305
18. Jiang, M. et al. J 2020 a novel ultrathin single-crystalline Bi₂O₃ nanosheet wrapped by reduced graphene oxide with improved electron transfer for Li storage. *J. Solid State Electrochem.* **24** 2487–2497
19. Yousefi, S., Ghasemi, B. & Nikolova, M. P. Morpho/Opto-structural characterizations and XRD-Assisted estimation of Crystallite size and strain in MgO nanoparticles by applying Williamson–Hall and size–strain techniques. *J. Cluster Sci.* **33**, 2197–2207 (2022).
20. Lim, D. J., Marks, N. A. & Rowles, M. R. Universal Scherrer equation for graphene fragments. *Carbon* **162**, 475–80 (2020).
21. Li, L., Zhang, M., Zhao, Z., Sun, B. & Zhang X 2016 Visible/near-IR-light-driven TNFePc/BiOCl organic-inorganic heterostructures with enhanced photocatalytic activity. *Dalton Trans.* **45**, 9497–9505
22. El-Newehy, M. H., El-Mahalawy, A. M., Thamer, B. M. & Moydeen Abdul Hameed, M. Fabrication and characterization of eco-friendly thin films as potential optical absorbers for efficient multi-functional opto-(electronic) and solar cell applications. *Materials* **16** (2023).
23. Aziz, S. B. et al. Characteristics of Poly(vinyl Alcohol) (PVA) Based Composites Integrated with Green Synthesized Al³⁺-Metal Complex: Structural, Optical, and Localized Density of State Analysis *Polymers* **2021**, Vol. **13**, Page 1316 13 1316 (2021).
24. Haryński, Ł., Olejnik, A., Grochowska, K. & Siuzdak K 2022 a facile method for Tauc exponent and corresponding electronic transitions determination in semiconductors directly from UV-Vis spectroscopy data. *Opt. Mater.* **127**, 112205
25. Modibane, K. D. et al. Poly(3-aminobenzoic acid) decorated with cobalt zeolitic benzimidazolate framework for electrochemical production of clean hydrogen. *Polymers* **12**, 1581 (2020).
26. Perveen, A. et al. W 2023 In-situ fabricated and plasmonic enhanced MACsPbBr₃-polymer composite perovskite film based UV photodetector. *J. Mol. Struct.* **1279** 134962
27. Qi, J. et al. Optimization of Broad-Response and High-Detectivity Polymer Photodetectors by Bandgap Engineering of Weak Donor-Strong Acceptor Polym. *Macromol.* **48**, 3941–3948 (2015).

28. Sendi, R. K., Al-Harbi, N., Atta, A., Rabia, M. & Abdelhamied, M. M. Copper oxide and copper nanoparticles insertion within a PPy matrix for photodetector applications. *Opt. Quant. Electron.* **55**, 1–15 (2023).
29. Liu, K., Sakurai, M., Liao, M. & Aono, M. Giant improvement of the performance of ZnO nanowire photodetectors by au nanoparticles. *J. Phys. Chem. C.* **114**, 19835–19839 (2010).
30. Atta, A. et al. Characterization and linear/non-linear optical properties of polypyrrole/NiO for optoelectronic devices. *Inorg. Chem. Commun.* **152**, 110726 (2023).
31. Bai, Z. & Zhang, Y. Self-powered UV-visible photodetectors based on ZnO/Cu₂O nanowire/electrolyte heterojunctions. *J. Alloys Compd.* **675**, 325–330 (2016).
32. Kalra, A. et al. Demonstration of high-responsivity epitaxial β -Ga₂O₃/GaN metal-heterojunction-metal broadband UV-A/UV-C detector. *Appl. Phys. Express.* **11**, 064101 (2018).
33. Wang, S. B. et al. R 2011 a CuO nanowire infrared photodetector. *Sens. Actuators A: Phys.* **171** 207–211
34. Naldoni, A. et al. Broadband hot-electron collection for solar water splitting with plasmonic titanium nitride. *Adv. Opt. Mater.* **5** (2017).
35. Tan, W. C., Shih, W. H. & Chen, Y. F. A highly sensitive Graphene-Organic Hybrid Photodetector with a Piezoelectric substrate. *Adv. Funct. Mater.* **24**, 6818–6825 (2014).
36. Hong, Q. et al. Self-powered ultrafast broadband photodetector based on p-n heterojunctions of CuO/Si nanowire array. *ACS Appl. Mater. Interfaces.* **6**, 20887–20894 (2014).
37. Popoola, A. J. et al. Carbon dopants carriers facilitators as agents for improving hole extraction efficiency of cobalt tetraoxide nanoparticles employed in fabrication of photodetectors. *Mater. Res. Bull.* **141**, 111331 (2021).
38. Zheng, L., Hu, K., Teng, F. & Fang, X. Novel UV-visible photodetector in photovoltaic mode with fast response and ultrahigh photosensitivity employing Se/TiO₂ nanotubes heterojunction. *Small* **13** (2017).
39. Costas, A. et al. I 2019 Radial heterojunction based on single ZnO-Cu_xO core-shell nanowire for photodetector applications *Sci. Rep.* **9**, 1–9.

Acknowledgements

The authors extend their appreciation to the Deanship of Scientific Research and Libraries in Princess Nourah bint Abdulrahman University for funding this research work through the Research Group project, Grant No. (RG-1445-0010)

Author contributions

This manuscript is produced under the sharing from all authors: writing, experimental, analyses are performed by Fatemah H. Alkallas, Mohamed Rabia, Fedor V. Kusmartsev, Amira Ben Gouider Trabelsi and all authors approve this submission.

Funding

This research was funded by the Deanship of Scientific Research and Libraries in Princess Nourah bint Abdulrahman University for funding this research work through the Research Group project, Grant No. (RG-1445-0010)

Declarations

Competing interests

The authors declare no competing interests.

Additional information

Correspondence and requests for materials should be addressed to A.B.G.T.

Reprints and permissions information is available at www.nature.com/reprints.

Publisher's note Springer Nature remains neutral with regard to jurisdictional claims in published maps and institutional affiliations.

Open Access This article is licensed under a Creative Commons Attribution-NonCommercial-NoDerivatives 4.0 International License, which permits any non-commercial use, sharing, distribution and reproduction in any medium or format, as long as you give appropriate credit to the original author(s) and the source, provide a link to the Creative Commons licence, and indicate if you modified the licensed material. You do not have permission under this licence to share adapted material derived from this article or parts of it. The images or other third party material in this article are included in the article's Creative Commons licence, unless indicated otherwise in a credit line to the material. If material is not included in the article's Creative Commons licence and your intended use is not permitted by statutory regulation or exceeds the permitted use, you will need to obtain permission directly from the copyright holder. To view a copy of this licence, visit <http://creativecommons.org/licenses/by-nc-nd/4.0/>.

© The Author(s) 2025